TCAD-Assisted MultiPhysics Modeling & Simulation for Accelerating Silicon Quantum Dot Qubit Design

F. A. Mohiyaddin, G. Simion, N. I. Dumoulin Stuyck*, R. Li, A. Elsayed#, M. Shehata#, S. Kubicek, C. Godfrin, B. T. Chan, J. Jussot, F. Ciubotaru, S. Brebels, F. M. Bufler, G. Eneman, P. Weckx, P. Matagne, A. Spessot, B. Govoreanu & I. P. Radu

imec, Kapeldreef 75, Leuven, B-3001, Belgium

* also with Department of Materials Engineering (MTM), KU Leuven, Kasteelpark Arenberg 44, Leuven, B-3001, Belgium

also with Department of Physics and Astronomy, KU Leuven, Celestijnenlaan 200d, Leuven, B-3001, Belgium

fahd.ayyalil.mohiyaddin@imec.be

***Abstract* — We summarize the design parameters and modeling techniques for silicon quantum dot qubit devices. A general overview on the operation of the devices - including various methods of qubit readout, control, and interaction - is provided with relevant parameters. With these blocks forming the backbone of silicon quantum computation, the paper provides a guideline to aid and accelerate the design and optimization of silicon qubit devices.**

Keywords*— *Silicon Quantum Computation, Device Design, Qubit Readout, Control & Interaction, Multiphysics Modeling.

I. Introduction

Over the last decade, Quantum Computers (QCs) have undergone a rapid transformation from lab-based devices satisfying academic curiosity to much larger-scale fab devices integrated with sophisticated control electronics [1-4]. Widespread interest in the development of quantum processors is evident, with several qubit platforms and novel operation methods being investigated [5]. While remarkable progress has been achieved towards the development of QC, the requirements of scalable fault-tolerant quantum computers [6] pose huge breakthroughs in the engineering of materials, process-integration, cryogenic control-electronics, and software. Device design methodologies are crucial for scaling up existing qubit demonstrations to larger-scale quantum computers, where the impact of several design parameters on the qubits need to be systematically investigated for better device operation, reproducibility, and yield.

Of several implementations, qubits based on silicon Quantum Dots (QDs) offer the advantages of compactness, long coherence times, elevated operation temperatures, and fabrication compatibility with techniques used in the semiconductor industry [7]. Silicon QD devices consist of "multi-gated transistors", where the gates are biased to confine a single electron in a quantum well potential, formed in the proximity of a material interface, typically Si/SiO_2 or Si/SiGe. The electron spin orientation with respect to an external static magnetic field B_0 constitutes the qubit. To be functional, spin-based QCs require blocks that demonstrate high-fidelity spin readout, control, and interaction over different length scales [8]. In this work, we present an overview on the operation and design of silicon QD qubits, including the various building blocks, design parameters and modeling techniques.

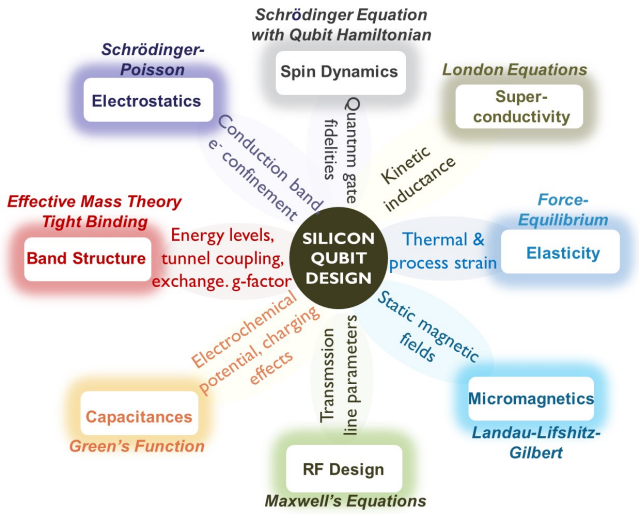

Fig. 1. Summary of all modeling parameters and techniques for designing silicon qubits devices, indicating the requirement of a multiphysics simulation approach.

II. Design of Silicon Qubit Devices

A. Requirement for a MultiPhysics Modeling Strategy

The operation of silicon qubit devices covers various aspects, and cannot be captured with a single design tool, requiring a multiphysics simulation approach [9]. For instance, the electron confinement is dependent on the potential landscape in the device (Section II.B), whereas spin readout is based on capacitances and tunnel interactions (Section II.C). Spin control is based on magnetic resonance with electromagnetic fields arising from transmission line antennas and magnets, requiring RF and magnet design respectively (Section II.D). The default interaction between electron spins is the short-range exchange interaction, necessitating sophisticated band-structure calculations (Section II.E). Medium- and long-range coupling employs dipolar interaction and microwave resonators respectively, requiring detailed understanding of the coupling mediators (Section II.E). Furthermore, additional effects such as noise (Section II.F), thermal strain and superconductivity (Section II.G) must be taken into consideration for device design. Fig. 1 shows a summary of all the modeling parameters for designing spin qubits, and the physical relations to build the models. We will now sequentially discuss devices that can host QD spin qubits, emphasizing key parameters and design considerations.

B. Electrostatic Confinement & Electron Energy Levels

As mentioned before, silicon qubits are defined in a quantum well potential at a material interface (Fig. 2a) [7]. The electron confinement and electrostatic potential can be estimated by solving the Schrödinger-Poisson (SP) equations self-consistently at low temperature with TCAD simulators. We note that appropriate choice of boundary conditions, meshes, truncation of extremely

small electron densities, and ramping down solutions from higher temperatures, can improve convergence significantly at low (~ 10 K) temperatures [10]. The spatial extent of the dots in the single-electron regime typically spans ~ 5 nm in the vertical direction perpendicular to the interface, and few tens of nm in the lateral direction [9]. This confinement leads to energy separations $\delta_O \sim 3 - 5$ meV between the ground (s-orbital) and excited (p-orbital) states (Fig. 2c), and is obtainable from SP solvers.

The degeneracy of the silicon conduction band minima leads to additional states (valley states) that negatively interfere with qubit operation (Fig. 2b). These states and the resultant splitting (valley splitting) between them are not captured fully in most SP solvers that rely on conventional effective mass theory. To capture such effects, the TCAD potentials are fed into detailed band-structure solvers that consider atomistic details at the interface. These solvers include (i) atomistic tight-binding methods [11] or (ii) modified versions of effective mass theory, where the TCAD wave-functions are combined with the silicon lattice Bloch functions (obtained from Density Functional Theory) to estimate valley splitting [12]. The valley splitting can be shown to be dependent on the interface step potential, vertical electric field in the dot, atomistic imperfections such as roughness and step edges, and typically varies between 50 – 200 μeV and 300 – 700 μeV in Si/SiGe and Si/SiO_2 devices respectively [13,14].

In the presence of a static magnetic field B_0, the spin (qubit) states of the electron in the dot are split in energy by the Zeeman Splitting $E_{ZS} = g_e \mu_B B_0$, where $g_e \sim 2$ is the electron g-factor and μ_B is the Bohr magneton (Fig. 2d). All the relevant energy separations are summarized in the table of Fig. 2, with values chosen to ensure that the qubit states are well separated from the excited orbital & valley states, for an isolated two-level qubit system.

C. *Electron Spin Readout*

The charge state of the electron in the dot acts as a handle for reading out the electron spin qubit. The process of spin readout starts with spin-dependent tunneling of the dot electron to an adjacent reservoir or to an ancilla dot, and the subsequent detection of the presence or absence of the dot electron with a charge sensor.

The first step of spin-dependent tunneling to a *reservoir* requires E_{ZS} to be much larger than the thermal broadening δ(T) of the reservoir's Fermi level, with a suitable choice of $B_0 \sim 1$ T [15]. This provides a good contrast between a spin ↑ electron tunneling to the reservoir, when compared to a spin ↓ electron remaining in the dot (Fig. 3b). The reservoir can also be replaced with an *ancilla dot*, containing an electron with spin initialized as ↓ [16]. The Pauli spin-exclusion principle then facilitates spin-dependent tunneling of the dot electron to the ancilla dot (Fig. 3b). The relevant design parameter here is the energy spacing ($\Delta_{ST} \sim \delta_{VS}$) in the ancilla dot, which needs to be sufficient to prevent thermal excitations.

A schematic of a charge sensor for charge detection in the dot is shown in Fig. 3a. The sensor is biased in a regime, where the current passing through the sensor is strongly sensitive to its electrostatic vicinity [15]. In this regime, the resulting change (Δ_μ) in the electrochemical potential (and thereby the sensor current) with the presence or absence of the QD electron (Fig. 3c) allows single-charge detection, and hence spin readout. A critical requirement here is a large capacitance between the QD and sensor, such that Δ_μ is not screened out by thermal broadening δ(T) of the Fermi level in the sensor [9]. For good charge detection fidelities, a sufficient on current ($I_{DS} \sim 1$ nA) is also required across the sensor, and is achievable with large tunnel rates ($\Gamma_S \sim 10$ GHz) and source drain bias ($V_{DS} \sim 1$ meV). Furthermore, the tunnel rate ($\Gamma_{dot} \sim 10$ kHz) of the QD electron to the reservoir or ancilla dot needs to be in the right range for good fidelities in reasonably short timescales.

A resonator (lumped or transmission line), directly connected to the gate above the readout dot [17], can also be used for charge detection (Fig. 3d). By appropriately biasing the dots, the resonator capacitance (and hence its resonant frequency) can be made dependent on the electron occupation in the readout dot, which further depends on the spin. The electron spin state can then be read out via the resonator reflectance. The change ($\Delta\nu_0$) in the resonator

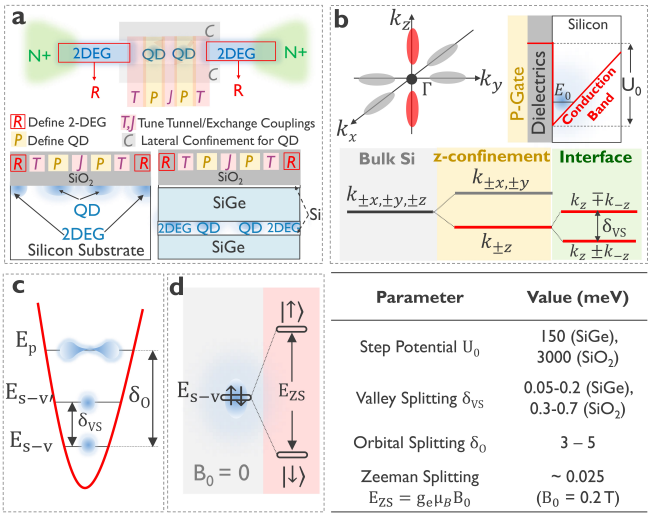

Parameter	Value (meV)
Step Potential U_0	150 (SiGe), 3000 (SiO_2)
Valley Splitting δ_{VS}	0.05-0.2 (SiGe), 0.3-0.7 (SiO_2)
Orbital Splitting δ_0	3 – 5
Zeeman Splitting $E_{ZS} = g_e \mu_B B_0$	~ 0.025 (B_0 = 0.2 T)

Fig. 2 (a) Schematic of accumulation-mode qubit devices based on Si/SiO_2 and Si/SiGe interfaces. (b) Multivalley nature of silicon conduction band and breaking of valley-degeneracies when an electron is confned at the interface. (c) Device potential sketch with different orbital energy levels. (d) Qubit energy levels in a static magnetic field B_0. (Table) Summary of relevant energy separations in the QD.

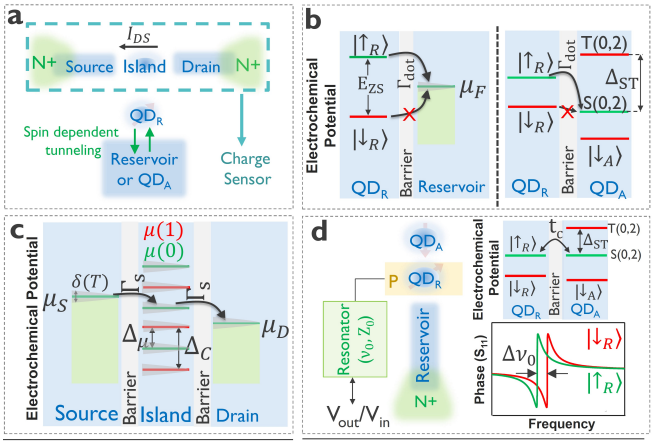

Sensor Parameters	Value
Source-Drain Bias V_{DS}	~ 1 mV
SET on Current I_{DS}	~ 1 nA
Sensor Tunnel Rate Γ_S	~ 10 GHz
Charging Energy Δ_C	~ 4 meV
Change in Electrochemical Potential Δ_μ	~ 200 μeV
Thermal Broadening δ(T) (T = 100 mK)	~ 40 μeV

Spin dependent Tunneling Parameters	Value
Dot to reservoir/ancilla dot tunnel rate Γ_{dot}	~ 10 kHz
Zeeman Splitting E_{ZS} (reservoir, ancilla dot)	~ 120 μeV, ~ 25 μeV
Singlet-Triplet Splitting $\Delta_{ST} \sim \delta_{VS}$	0.05-0.7 meV
Resonator based Readout Parameters	**Value**
Resonator Frequency Change $\Delta\nu_0$ (Z_0 = 1.2 kΩ, ν_0 = 5.6 GHz, t_c = 10 GHz, α = 0.1)	~ 2 MHz

Fig. 3. (a) Schematic indicating the position of the charge sensor, quantum dots and reservoir for spin readout. (b-c) Alignment of electrochemical potentials for (b) spin-dependent tunneling, and (c) charge sensing. μ(N) is the electrochemical potential in the island, N is electron number in the dot (d) Spin readout with a resonator via reflectometry. (Tables) Summary of design parameters for readout.

frequency can be shown to depend on the difference (α) of the lever arms of the resonator to the dots, the resonator characteristic impedance Z_0, frequency ν_0, and the interdot tunnel coupling t_c [17]. For sufficient readout contrast, these parameters are chosen such that $\Delta\nu_0$ is comparable to or larger than the resonator line width ν_0/Q, where Q is the resonator quality factor.

All readout methods involve capacitances, which can be extracted with standard capacitance simulation software. These capacitances can be fed into Monte-Carlo circuit simulators to model current transport across charge sensors. For the tunnel rates, a WKB approximation provides the required barrier heights (few 100 μeV) and barrier dimensions (few tens of nm) [9]. Estimation of interdot tunnel couplings involve modeling energy levels in a double QD system, obtainable with standard SP solvers. For dispersive readout, it is crucial to model the resonator frequencies and impedances, for which the Maxwell's equations are solved.

D. *Electron Spin Control*

For spin control, the electron is subject to an RF magnetic field, whose direction is perpendicular to that of the static field B_0. Under the resonance condition, where the frequency of the RF field is equivalent to E_{ZS}, the electron spin state rotates between ↑ and ↓ states with a Rabi frequency f_R proportional to the RF field amplitude B_{ac}. The effective RF field can be generated either by a transmission line (resulting in Electron Spin Resonance), or by displacing the electron electrically in a magnetic field gradient b_c (resulting in Electric Dipole Spin Resonance). The former method involves a microwave transmission line with a node, such that the RF magnetic fields experienced by the electron is maximized, while ensuring minimal RF electric fields (Fig. 4a). The transmission line also needs to be impedance matched, for maximal B_{ac} at the qubit location. Assuming an input power $P_{ac} \sim 1\mu W$, a field amplitude $B_{ac} \sim 80\ \mu T$ is achievable at the qubit position, yielding Rabi frequencies $f_R \sim 1$ MHz [18].

The second method involves placing magnets near the electron qubits, and electrically shifting the electron in the resultant magnetic field gradient (Fig. 4b) [19]. The magnetic fields and their gradients are obtainable by solving the Landau-Lifshitz-Gilbert equations. The field gradients will be present in different directions, some (b_c) facilitating qubit control, while the others (b_d) result in spin dephasing. The design needs to ensure a large value of b_c (typically ~ 0.35 mT/nm), while keeping b_d minimal. The shift in the electron position with gate voltages can be modeled with SP solvers, and is ~ 1 nm for voltage amplitudes $V_{ac} \sim 200$ mV in single QDs, yielding $f_R \sim 5$ MHz [9].

To achieve similar or larger Rabi frequencies with lower drive voltages, the electron can be further delocalized in a double QD (Fig. 4c) [20]. Quantum mechanically, this strongly couples the electron spin with its position via the magnetic field gradient, in addition to creating a charge dipole that is strongly sensitive to gate voltages. This picture can be simplified with a transformation (Schrieffer-Wolff (SW)) to yield a Rabi frequency f_R dependent on field gradient b_c, interdot tunnel coupling t_c, and difference α in lever arms. With an appropriate choice of parameters, $f_R \sim 25$ MHz is achievable at much smaller voltage amplitudes $V_{ac} \sim 30\ \mu V$.

Note that the electron spin resonance frequency and coherence depend on the stability of g-factor g_e, which is related to the spin-orbit interaction (SOI). Tight-binding and extensions of effective mass theory have been extensively used to estimate SOI in qubit devices [21]. It can be shown that SOI is strongly sensitive to atomistic interface details, when B_0 is aligned parallel to the interface, leading to non-uniform (by ~ 1%) qubit frequencies. This is overcome by aligning B_0 perpendicular to the interface.

Finally, we highlight that the ability to readout and control the qubit will also provide the capability for deterministic qubit initialization.

E. *Coupling Electron Spins*

The interaction between electron spins in a double QD is the exchange coupling J_e, which is a short-range mechanism depending on the overlap between the orbital wave-functions in the dots (Fig. 5a) [22]. J_e is estimated by first calculating the device potential with SP solvers, feeding the potential into band-structure calculators to estimate orbital wave functions, and combining them with computational chemistry techniques. For two qubit operations, it is essential to tune J_e by either (i) varying the tunnel barrier between the two dots, or by (ii) shifting the relative energies (i.e. by a detuning) between the dots. Both methods yield several orders of magnitude tunability (1 MHz - 1 GHz) of J_e, when the tunnel barriers and relative energies are tuned by several hundred μeV [9].

For medium range coupling, the spin-spin interaction can be mediated by the charge dipoles. Each electron is then delocalized in a double QD in the presence of a magnetic field gradient (Fig. 5b). The electron spin is then coupled to its position that constitutes a charge dipole (Fig. 4c) [20]. Two such dipoles are then coupled via the dipolar interaction, yielding an indirect spin-spin interaction [23]. The strength D_e of the interaction can be estimated with a SW transformation, and depends on the field B_0, field gradient b_c, interdot tunnel coupling V_t, interdot distance L, and dipole separation r [23]. An optimal choice of parameters yields $D_e \sim 3$ MHz between qubits that are separated by as far as 500 nm. Note that the interaction can also be turned off by localizing the electron qubits in a single QD.

As charge dipoles are very sensitive to electric fields and voltages, they can be coupled to a resonator mode via the resonator vacuum voltage V_{vac} (Fig. 5c) [24]. This leads to an indirect

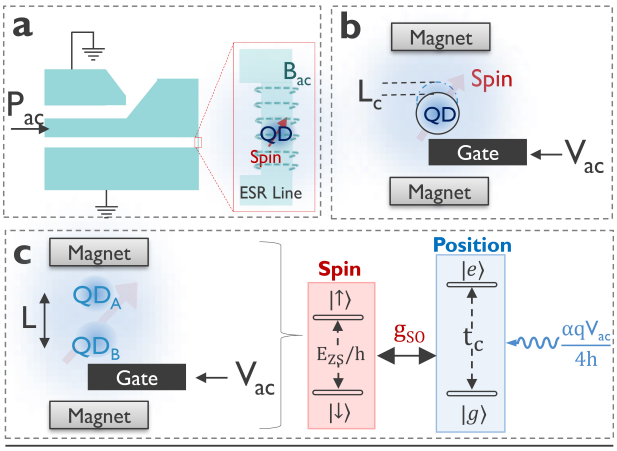

Parameter	Assumptions	Value (MHz)
Rabi Frequency (ESR)	$P_{ac} = 1\ \mu W$, $Z_0 = 50\ \Omega$	~1
Rabi Frequency (EDSR in Single QD)	$b_c = 0.35$ mT/nm, $L_c = 1$ nm ($V_{ac} = 200$ mV)	~ 5
Electron Spin-Position Coupling Strength g_{SO} (in Double QD)	$b_c = 0.35$ mT/nm, L = 100 nm	~ 250
Rabi Frequency (EDSR in Double QD)	$B_0 = 0.2$ T, $t_C = 10$ GHz, $\alpha = 0.1$, $V_{ac} = 30\ \mu V$, $g_{SO} = 250$ MHz	~ 25

Fig. 4. Spin control methods based on (a) Electron Spin Resonance (ESR) with a transmission line antenna, (b-c) Electric Dipole Spin Resonance (EDSR) in a (b) single QD and (c) double QD. h is the Planck constant and q is elementary charge. (Table) Summary of all design parameters and Rabi frequencies for the control methods. Note : Energy splittings and coupling strengths are in units of frequency.

coupling between the spin and resonator. Two spins coupled to the resonator can then be coupled with each other. The effective spin-spin interaction strength P_e via the resonator can be estimated with SW transformations and depends on several parameters summarized in the table of Fig. 5 [24]. An appropriate choice of parameters, obtained by using high-impedance resonators, yields $P_e \sim 0.3$ MHz between spins that are separated by few mm. The resonator can also be used to readout the spin via the reflectometry techniques described in Section II.C. The difference here is that an ancilla spin is not necessary for readout, as the spin states are directly coupled to the resonator. The design of structures involving dipolar- or resonator-based coupling requires modeling magnetic field gradients, electrostatic potentials, tunnel couplings and resonator parameters in addition to transformations, such as SW.

F. Electromagnetic Noise

Noise arises from several sources including Johnson noise, imperfections in the magnets, charge defects, thermal fluctuations, and magnetic (e.g. Si-29) impurities [14]. Popular noise minimization techniques involve attenuation of DC lines, reducing magnet vibrations, driving qubits at smaller RF powers, and using isotopically purified Si-28 substrates [14, 25]. However, a detailed investigation of all noise sources, especially electric field noise E_n, is impractical, due to lack of experimental evidence on their origin. Hence, empirical values of E_n (~ 100 V/m) and spin-coherence times (~1 – 100 μs), along with realistic parameters summarized in all the tables, are often fed into simplified qubit Hamiltonians, where the Schrodinger and Master Equations are solved to estimate the qubit dynamics and fidelity of quantum gate operations.

The sensitivity of qubits to noise can be reduced with proper device design. For example, aligning B_0 perpendicular to the interface renders the g-factor g_e insensitive to vertical electric fields, and thereby a component of noise [21]. Optimal magnet design to ensure an extremely small and robust dephasing gradient b_d can also enhance coherence times [24]. This is critical when the qubits are delocalized in double QDs for fast control or long-distance interaction, where they are made sensitive to the electric field.

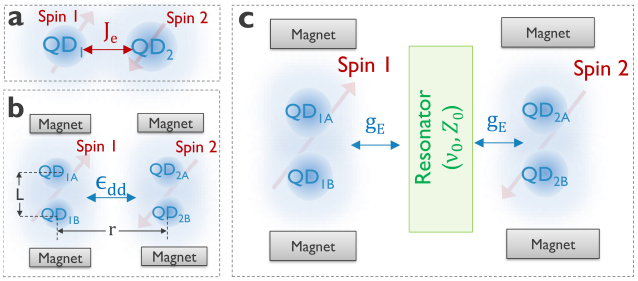

Parameter	Assumptions	Value (MHz)
Spin-Spin Coupling Strength J_e via Exchange Interaction	Qubit pitch r ~ 80 nm	~ 1 – 1000
Electron Spin - Position Coupling Strength g_{SO} in a double QD	b_c ~ 0.35 mT/nm, Dot pitch L = 100 nm	~ 250
Dipolar Coupling Strength ϵ_{dd} between Electron Positions	L = 100 nm, r ~ 500 nm	~ 600
Spin-Spin Coupling Strength D_e via Dipolar Interaction	B_0 = 0.2 T, t_C= 10 GHz, g_{SO} = 250 MHz, ϵ_{dd} = 600 MHz	~ 3
Coupling Strength g_E between Electron Position and Resonator	α = 0.1, ν_0 = 5.65 GHz, Z_0 ~ 1.2 kΩ, (V_{vac} ~ 10 μV)	~ 60
Spin-Spin Coupling Strength P_e via Resonator-Mediated Interaction	B_0 = 0.2 T, t_C = 10 GHz, g_{SO} = 250 MHz, g_E = 60 MHz	~ 0.3

Fig. 5. Coupling of spin qubits via (a) short-range exchange interaction, (b) medium-range dipolar interaction, and (c) resonators facilitating long-range interaction. (Table) Summary of design parameters and coupling strengths for the three methods. Note : All coupling strengths are expressed in units of frequency.

Under such operation regimes, the design parameters are also chosen to minimize spin dephasing effects via the position and resonator. Operating the qubits in certain biasing conditions may also render the qubit in-sensitive to noise, as noise affects the qubit frequency via different pathways, that could cancel out [20]. In addition to device design, utilizing sophisticated pulsing protocols can further mitigate the impact of noise on the qubits [26].

G. Other Low Temperature Considerations

Thermal strain has been shown to modify the conduction band by few meV in the QDs and their vicinity [27], and can be modeled with TCAD process and device simulators. The requirement of small barrier heights (~ few 100 μeV) between the QDs/reservoirs for qubit operations necessitates extremely small values of strain gradients in the barriers. This is achievable with appropriate choice of gate materials (e.g. Polysilicon) and device geometries [9].

Another cryogenic effect is superconductivity, which plays a significant role in the design of transmission lines and resonators for qubit readout, control, and coupling. The key parameter is the kinetic inductance L_k of materials and can be included in RF simulations by assuming an analytical derived value of the sheet inductance [28]. A large value of L_k (few tens of nH) is generally chosen for good readout contrast and strong qubit coupling via high-impedance resonators. On the contrary, L_k needs to be minimized for the qubit to be controlled with maximal B_{ac}.

III. SUMMARY

Based on a multiphysics modeling strategy, we have provided a general guideline on the interplay between various design parameters for silicon qubit structures. These guidelines can be used for designing optimal silicon qubit devices with spin readout, control, and coupling. We foresee that the modeling techniques constitute a design framework that will play a pivotal role in scaling up existing qubit prototypes to larger-scale quantum processors.

REFERENCES

[1] F. Arute et al., *Nature*, 574, 505-510, 2019.
[2] R. Pillarisetty et al., *Proceedings of IEDM*, 2018.
[3] B. Govoreanu et al., *Proceedings of SNW*, 2019.
[4] D. J. Dean et al., Quantum Information Science, *Factual Document for the Office of Basic Energy Sciences at the Department of Energy*, 2017.
[5] T. S. Humble et al., *IEEE Design & Test*, 36, 3, 2019.
[6] A. Fowler et al., *Physical Review A*, 86, 032324, 2012.
[7] L. M. K. Vandersypen et al., *npj Quantum Information*, 3, 34, 2017.
[8] D. Divincenzo, *Fortschritte der Physik:Progress of Physics*, 48, 2000.
[9] F. A. Mohiyaddin et al., *Proceedings of IEDM*, 2019.
[10] F. A. Mohiyaddin et al., *Proceedings of COMSOL Conference*, 2017.
[11] R. Rahman et al., *Physical Review B*, 83, 239904, 2011.
[12] J. K. Gamble et al., *Applied Physics Letters*, 109, 253101, 2016.
[13] C. H. Yang et al., *Nature Communications*, 4, 2069, 2013.
[14] F. A. Zwanenburg et al., *Reviews of Modern Physics*, 85, 961, 2013.
[15] M. Veldhorst et al., *Nature Nanotechnology*, *9*, *981-985,* 2014.
[16] N. W. Hendrickx et al., *Nature Communications*, 11, 3478, 2020.
[17] A. C. Betz et al., *Nano Letters*, 15, 7, 4622-4627, 2015.
[18] J. P. Dehollain et al., *Nanotechnology*, 24, 1, 2013.
[19] J. Yoneda et al., *Nature Nanotechnology*, 13, 102-106, 2018.
[20] M. Benito et al., *Physical Review B*, 100, 125430, 2019.
[21] R. Ferdous et al., *Physical Review B*, *97*, 241401, 2018.
[22] Q. Li et al., *Physical Review B*, 81, 085313, 2010.
[23] J. Cayao et al., *Physical Review B*, 101, 195438, 2020.
[24] F. A. Mohiyaddin et al., *Proc. of IITC*, 2019.
[25] J. P. G. Van Dijk et al., *Physical Review Applied*, 12, 044054, 2019.
[26] S. Machnes et al., *Physical Review A*, 84, 022305, 2011.
[27] T. Thorbeck et al., *AIP Advances*, 5, 087107, 2015.
[28] E. F. C. Driessen et al., *Physical Review Letters*, 109, 107003, 2012.